Rollocopter: An Energy-aware Hybrid Aerial-ground Mobility for Extreme Terrains

Sahand Sabet
Department of Aerospace and Mechanical Engineering
University of Arizona
Tucson, AZ 85719
(480) 703-9396
sahandsabet@email.arizona.edu

Ali-akbar Agha-mohammadi
Jet Propulsion Laboratory
California Institute of Technology
Pasadena, CA 91109
(626) 840-9140
aliagha@jpl.nasa.gov

Andrea Tagliabue
Jet Propulsion Laboratory
California Institute of Technology
Pasadena, CA 91109
(510) 701-4579
andrea.tagliabue@jpl.nasa.gov

D. Sawyer Elliott
Department of Aerospace Engineering
Cornell University
ITHACA, NY 14853
(607) 255-1805
dse44@cornell.edu

Parviz E. Nikravesh
Department of Aerospace and Mechanical Engineering
University of Arizona
Tucson, AZ 85719
(520) 626-2053
pen@email.arizona.edu

***Abstract*— In this work, we design and model a new hybrid aerial-ground mobility system for extreme terrains referred to as Rollocopter. The platform uses common multi-rotor propellers enclosed in a spherical shell to produce the necessary forces to roll on the ground and fly. The proposed platform is able to achieve (a) multi-modal locomotion (fly and roll) for increased energy efficiency, (b) collision resiliency due to its impact-resistant structure, and (c) high-level of controllability due to three-dimensional actuation. This work focuses on the preliminary design trade-offs, analysis and feasibility assessment of the platform. First, a dynamic model of the robot that considers interaction with the ground is developed. Second, a control architecture for flying and rolling is proposed and evaluated in simulation. Finally, a discussion on the energy efficiency of the flying and rolling mobility modes via leveraging a derived dynamic model of the power consumption is provided.**

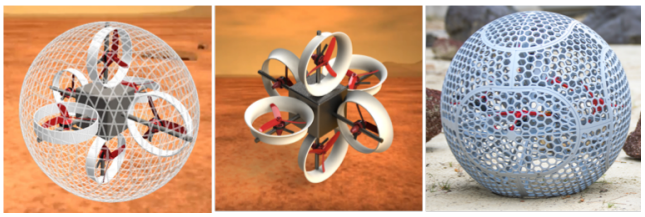

Figure 1: Left: Rollocopter concept art, including propellers, electronics (gray box) and the impact-resilient cage. Middle: hexacopter configuration of the propellers. Right: A Rollocopter prototype. The spherical cage allows to roll on flat terrains and to be impact-resistant, while the configuration of the propellers guarantees actuation in any direction.

TABLE OF CONTENTS

1. INTRODUCTION

Over the past years, Micro Aerial Vehicles (MAVs) have been increasingly considered for various applications, ranging from search and rescue [1], [2], agriculture [3] or aerial deliveries [4], [5]. Recently, thanks to their relatively simple mechanical design and availability of components, MAVs are also gaining interest for space applications, focused on the exploration of space bodies with an atmosphere [6], [7], [8]. However, the deployment of small multi-rotorcrafts in the real-world application is still limited. This limitation is due to challenges in expanding the autonomy in terms of range and ability to interact and traverse different environments.

Autonomy of MAVs, in terms of flight time or distance, is constrained by the aerodynamics of flight itself and the required energy for constantly defeating gravity. These limitations are usually overcome via mechanical improvements [9], designing platforms with optimized weight, or by deploying hybrid solutions such as Vertical Take-Off and Landing (VTOL) robots [10] or platforms capable of flying and rolling [11]. The ability to negotiate obstacles and difficult terrains, instead, is usually addressed by designing platforms equipped with a protective cage or shell which shields the fragile propellers and electronics from unexpected impacts with the environment [11], [12]. Increased autonomy in terms of possibilities of interaction with the environment is typically achieved by equipping the robots with dexterous manipulators [13], or by designing novel omni-directional copters that can fly with any desired attitude [14], [15].

978-1-5386-6854-2/19/$31.00 ©2019 IEEE

Figure 2: Artist's representation of the Shapeshifter [8] platform self-assembling to the Rollocopter shape. The Shapeshifter is a multi-modal and multi-agent platform for the exploration of planets and their moons with an atmosphere, such as Titan.

In this work, we propose a novel rotorcraft (see Figure 1), referred to as Rollocopter that is able to (a) extend its maximum range by choosing to fly or roll on the ground, (b) withstand small impacts/contacts with the environments, and (c) produce force and torque in any direction, allowing it to fly with arbitrary attitude. The design of the Rollocopter is based on a set of six reversible propellers, in co-planar pairs, placed along three orthogonal axes. The placement of the propellers allows producing forces and torques in any direction, enabling it to fly at any attitude and to produce the necessary torques for rolling. The propellers are enclosed in a spherical shell that allows for airflow while protecting the propellers, batteries, and on-board electronics from impacts with the ground and the surrounding environment.

The objective of this paper is to present an initial trade-off study and feasibility analysis for the hardware implementation of the platform. We start by deriving the dynamics model of the robot taking into account the different mobility modes and capturing interaction with the ground. Then, we evaluate the ability to produce torque and forces in any direction. Second, we derive a control strategy for the flying and rolling mode. Finally, we present a comparison of the power requirement for rolling and flying, illustrating the increased range capability of the hybrid mobility system.

This work also paves the way for the next generation of modular UAVs, offering an alternative approach to the rolling mobility of the Shapeshifter conceptual platform [8], where a spherical rolling/flying shell consists of multiple self-assembling agents, with different propeller placements (Figure 2).

Outline The remainder of this paper is organized as follows: Section 2 describes the system and the derivation of a dynamics model which takes into account the rolling and flying mode. Section 3 presents a control strategy to track a desired position and attitude. Section 4 provides an energy efficiency analysis that compares the power consumption of the rolling and flying modes. We present the results in Section 5 and discuss the future work and concluding remarks in Section 6.

2. System Description and Dynamics Model

In this section, we present the Rollocopter design and derive a dynamics model for the rolling and flying mobility modes of the platform, taking into account the terramechanics of the rolling platform.

System Description: The six-degrees of freedom Rollocopter is comprised of a spherical cage that encloses a set of propellers, electronics, and a battery (Figure 1). In this work, we focus on a six propeller variant (hexacopter) of the Rollocopter. The hexacopter is fixed to the outer shell and the whole system translates/rotates together. The proposed configuration of the propellers enables actuation of all six degrees of freedom, while allowing for energy-saving rolling mobility mode.
Notation Declaration: $\boldsymbol{I}_n$ and $\mathbf{0}_{n\times m}$, respectively, denote a n-by-n identity matrix and a n-by-m matrix of zeros. Throughout the paper, vectors and matrices are distinguished by bold-face variables.

Coordinate Systems: In this work we define a body-fixed frame B_f (ξ-η-ζ) and an inertial frame I_f (X-Y-Z), shown in Figure 3. It is assumed that the body reference frame is centered in the Center of Mass (CoM) of the Rollocopter (same as the geometrical center).

Actuation System: The actuation system (shown in Figure 3) consists of a set of six reversible and fixed-pitch propellers that are distributed within the outer shell. The propellers have a fixed orientation with respect to the body-frame B_f (ξ-η-ζ). While the mass of the motors is included in the dynamics calculations, the propellers are assumed to be massless. Ignoring the propeller mass and the induced-velocity effects and viscous drag, the force $\boldsymbol{f}_{p_i}$ and torque $\boldsymbol{\eta}_{p_i}$ generated by the i-th propeller are:

$$\boldsymbol{f}_{p_i} = k_i\omega_i^2\boldsymbol{s}_i, \quad \boldsymbol{\eta}_{p_i} = \tilde{\boldsymbol{\rho}}_i\boldsymbol{f}_{p_i} \tag{1}$$

k_i and ω_i are the force constant and magnitude of the angular velocity of the i-th propeller. The term $\boldsymbol{s}_i \in R^3$ represents a unit vector normal to the propeller's disk (see Figure 3) and $\boldsymbol{\rho}_i \in R^3$ denotes the vector connecting the center of mass of the vehicle to the i-th propeller. The "$\sim$" sign on $\boldsymbol{\rho}_i$ represents the skew-symmetric matrix operator corresponding to the vector cross product ($\tilde{\boldsymbol{\rho}}_i\boldsymbol{f}_{p_i} = \boldsymbol{\rho}_i \times \boldsymbol{f}_{p_i}$) where

$$\tilde{\boldsymbol{\rho}}_i = \begin{bmatrix} 0 & -\boldsymbol{\rho}_{iz} & \boldsymbol{\rho}_{iy} \\ \boldsymbol{\rho}_{iz} & 0 & -\boldsymbol{\rho}_{ix} \\ -\boldsymbol{\rho}_{iy} & \boldsymbol{\rho}_{ix} & 0 \end{bmatrix} \tag{2}$$

Drag Force: An analytical model is used to calculate the array of aerodynamic drag force/torque as:

$$\begin{aligned} &\boldsymbol{g}_d = [\boldsymbol{f}_d^T, \boldsymbol{\eta}_d^T]^T, \\ &\boldsymbol{f}_d = -\frac{1}{2}\bar{\rho}_{den}C_dA_d||\boldsymbol{v}_f||^2\boldsymbol{u}_{\boldsymbol{v}_f}, \;\; \boldsymbol{u}_{\boldsymbol{v}_f} = \boldsymbol{v}_f||\boldsymbol{v}_f||^{-1}, \\ &\boldsymbol{\eta}_d = \mathbf{0}_{3\times 1} \end{aligned} \tag{3}$$

where C_d is the drag coefficient, $\bar{\rho}_{den}$ is the air density, A_d is the cross-sectional area of the Rollocopter, and $\boldsymbol{v}_f$ is the relative airstream velocity.

Thruster Allocation: With control signal defined as $\boldsymbol{u} = \left[\omega_1^2, \omega_2^2, \ldots, \omega_6^2\right]^T$, the aggregated force and torque applied to the system are found using Eq. 1

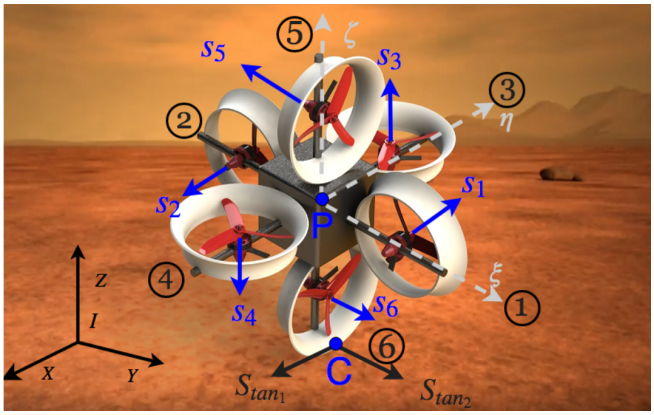

Figure 3: Rigid body diagram of the proposed Rollocopter design. For clarity, the protective shell is not shown. The point P represents the center of mass of the robot, while C the contact point with the terrain. I is the inertial reference frame.

$$\boldsymbol{g}_p = \begin{bmatrix} \boldsymbol{f}_p \\ \boldsymbol{\eta}_p \end{bmatrix} = \boldsymbol{T}\boldsymbol{u}, \quad \boldsymbol{T} = k \begin{bmatrix} \boldsymbol{s}_1 & \boldsymbol{s}_2 & \dots & \boldsymbol{s}_6 \\ \tilde{\boldsymbol{\rho}}_1 \boldsymbol{s}_1 & \tilde{\boldsymbol{\rho}}_2 \boldsymbol{s}_2 & \dots & \tilde{\boldsymbol{\rho}}_6 \boldsymbol{s}_6 \end{bmatrix},$$
$$\text{where } \boldsymbol{f}_p = \sum_{i=1}^{6} \boldsymbol{f}_{p_i}, \ \boldsymbol{\eta}_p = \sum_{i=1}^{6} \boldsymbol{\eta}_{p_i} \tag{4}$$

Matrix $\boldsymbol{T} \in R^{6\times 6}$ is a function of propellers' relative position $\boldsymbol{\rho}_i$, orientation $\boldsymbol{s}_i$ with respect to body-frame B_f, and the force constant k (assuming k_i is same for all propellers). In order to find the rank of the matrix $\boldsymbol{T}$, the unit vector normal to each propeller's disk, $\boldsymbol{s}_i$, is shown in Figure 3. The distance from the center of mass, P, to the center of each propeller is R_p. Consequently, the matrix $\boldsymbol{T}$ for the proposed configuration shown in Figure 3 can be simplified into

$$\boldsymbol{T} = k \begin{bmatrix} 0 & 0 & 0 & 0 & -1 & 1 \\ 1 & -1 & 0 & 0 & 0 & 0 \\ 0 & 0 & 1 & -1 & 0 & 0 \\ 0 & 0 & R_p & R_p & 0 & 0 \\ 0 & 0 & 0 & 0 & -R_p & -R_p \\ R_p & R_p & 0 & 0 & 0 & 0 \end{bmatrix} \tag{5}$$

where the i-th column in the matrix $\boldsymbol{T}$ corresponds to the i-th propeller (see propellers labels in Figure 3). For a fully controllable vehicle, which could generate force and torque in any direction, the rank of the matrix $\boldsymbol{T}$ should be at least six. With the proposed configuration of the propellers, the matrix $\boldsymbol{T}$ is full rank and hence the vehicle is fully controllable.

Equations of Motion: To compute the dynamics model of the robot, we express the equations of motion of the vehicle, subject to a set of kinematic constraints $\boldsymbol{\phi} = \boldsymbol{0}$, using Newton-Euler approach:

$$\begin{bmatrix} \boldsymbol{M} & \boldsymbol{0}_{3\times 3} \\ \boldsymbol{0}_{3\times 3} & \boldsymbol{J} \end{bmatrix} \begin{bmatrix} \ddot{\boldsymbol{r}}_{\boldsymbol{P}} \\ \dot{\boldsymbol{\omega}} \end{bmatrix} + \begin{bmatrix} -m\boldsymbol{g}_{gravity} \\ \tilde{\boldsymbol{\omega}}\boldsymbol{J}\boldsymbol{\omega} \end{bmatrix} = \boldsymbol{g}_d + \boldsymbol{g}_p + \delta\boldsymbol{g}_c. \tag{6}$$

where, m and $\boldsymbol{M} = m\boldsymbol{I}_3$, respectively, denote the Rollocopter's mass and mass matrix. The term $\boldsymbol{r_P} = [\boldsymbol{r}_{x_P}, \boldsymbol{r}_{y_P}, \boldsymbol{r}_{z_P}]^T$ represents the location of the center of mass and $\boldsymbol{\omega}$ is the angular velocity vector defined in the inertial frame I_f. The moment of inertia and the gravity vector are respectively denoted by $\boldsymbol{J}$ and $\boldsymbol{g}_{gravity} \in R^3$. The terms $\boldsymbol{g}_d$, $\boldsymbol{g}_p$, and $\boldsymbol{g}_c$ respectively represent the $R^{6\times 1}$ arrays of drag, propellers, and constraints forces/torque. When the vehicle is flying (no kinematic constraint), δ is zero, otherwise δ is one.

Lagrangian Dynamics Equations: To develop the set of kinematic constraints applied to the system $\boldsymbol{\phi}_i$, the points P and C are defined as shown in Figure 3. Point P is located at the center of mass of the vehicle and vector $\boldsymbol{r_C} = [\boldsymbol{r}_{x_C}, \boldsymbol{r}_{y_C}, \boldsymbol{r}_{z_C}]^T$ connects the origin to the contact point of the vehicle and the ground (it should be mentioned that the point C is defined on the ground not on the body). It is assumed that the terrain which the vehicle rolls on is defined as $Q(x_C, y_C, z_C) = z_C + H(x_C, y_C) = 0$. Q and H are smooth continuous functions.The set of kinematic constraints applied to the system $\boldsymbol{\phi}_i$ are written as:

$$\boldsymbol{\phi}_{1-3} = \boldsymbol{r_P} - \boldsymbol{r_C} - R\overline{\nabla Q} = \boldsymbol{0}_{3\times 1} \tag{7}$$
$$\overline{\nabla Q} = \frac{\nabla Q}{||\nabla Q||}$$
$$\dot{\boldsymbol{\phi}}_{4-6} = \tilde{\boldsymbol{\omega}}(\boldsymbol{r_P} - \boldsymbol{r_C}) - \dot{\boldsymbol{r}}_{\boldsymbol{P}} = \boldsymbol{0}_{3\times 1} \tag{8}$$

where Eq. 7 is the position loop relating $\boldsymbol{r_P}$ to $\boldsymbol{r_C}$. The term R denotes the radius of the sphere. The gradient of the terrain (a column vector $\in R^3$) and its normalized vector are denoted with ∇Q and $\overline{\nabla Q}$, respectively. The nonholonomic rolling constraints are provided in Eq. 8. To transfer the Newton-Euler dynamics equation provided in Eq. 6 to the Lagrange equations [16], the dependent coordinates need to be removed from the equations of motion. By taking derivative of Eq. 7 and rewriting Eq. 8, the kinematic constraints at the velocity level can be represented as

$$\dot{\boldsymbol{r}}_{\boldsymbol{P}} = \dot{\boldsymbol{r}}_{\boldsymbol{C}} + R\dot{\overline{\nabla Q}} \tag{9}$$
$$\dot{\boldsymbol{r}}_{\boldsymbol{P}} = \tilde{\boldsymbol{\omega}}(\boldsymbol{r_P} - \boldsymbol{r_C}) \tag{10}$$

Using Eq. 9, the vector $\dot{\boldsymbol{r}}_{\boldsymbol{P}}$ can be represented in terms of $\dot{\boldsymbol{r}}_{\boldsymbol{C}}$ or vice versa using transformation matrix $\boldsymbol{S}$

$$\dot{\boldsymbol{r}}_{\boldsymbol{P}} = \boldsymbol{S}\dot{\boldsymbol{r}}_{\boldsymbol{C}}$$
$$\boldsymbol{S} = [\boldsymbol{I_3} + R\underline{\boldsymbol{J}}(\overline{\nabla Q})] \tag{11}$$

where the term $\underline{\boldsymbol{J}}(\overline{\nabla Q}) \in R^{3\times 3}$ denotes the Jacobian of the vector $\overline{\nabla Q}$ where

$$\underline{\boldsymbol{J}}(\overline{\nabla Q})_{ij} = \frac{\partial \overline{\nabla Q}_i}{\partial x_j} \tag{12}$$

It can be observed that presenting $\dot{\boldsymbol{r}}_{\boldsymbol{P}}$ in terms of $\dot{\boldsymbol{r}}_{\boldsymbol{C}}$ will significantly reduce the complexity of the dynamics equations, since the inverse of the transformation matrix $\boldsymbol{S}$ will be highly nonlinear. The kinematic relation between $\boldsymbol{r_P}$ and $\boldsymbol{r_C}$ at the acceleration level can be found by taking the first time derivative of Eq. 11

$$\ddot{\boldsymbol{r}}_{\boldsymbol{P}} = \boldsymbol{S}\ddot{\boldsymbol{r}}_{\boldsymbol{C}} + \dot{\boldsymbol{S}}\dot{\boldsymbol{r}}_{\boldsymbol{C}} \tag{13}$$

By substituting Eq. 7 into Eq. 10, one can rewrite Eq. 10 as

$$\dot{\boldsymbol{r}}_{\boldsymbol{P}} = \tilde{\boldsymbol{\omega}}(R\overline{\nabla Q}) \tag{14}$$

After relating the position (Eq. 7), velocity (Eq. 9), and acceleration (Eq. 13) of the points P and C, the next step in finding Lagrange equation is to remove the array of unknown constraint force $\boldsymbol{g}_c$ from the dynamics equations provided in

Eq. 6. Using the nonholonomic constraint equation Eq. 14, the array of velocity $\boldsymbol{q} = [\dot{\boldsymbol{r}}_{\boldsymbol{P}}, \boldsymbol{\omega}]^T$ can be written in terms of the array of angular velocity $\boldsymbol{\omega}$ as

$$\begin{bmatrix} \dot{\boldsymbol{r}}_{\boldsymbol{P}} \\ \boldsymbol{\omega} \end{bmatrix} = \boldsymbol{B_0}\boldsymbol{\omega}, \boldsymbol{B_0} = \begin{bmatrix} -R\widetilde{\nabla Q} \\ \boldsymbol{I}_3 \end{bmatrix} \tag{15}$$

By left multiplying the matrix $\boldsymbol{B}_{\boldsymbol{0}}^T \in R^{3\times 6}$ to the equations of motions provided in Eq. 6, we can project the dynamics equation onto the space of admissible motion and eliminate the array of unknown constraint force $\delta \boldsymbol{g}_c$ [16]. By combining Eqs. 6 and 15, the equations of motion in the Lagrange's form can be found after some simplification as

$$\begin{aligned} \boldsymbol{B}_{\boldsymbol{0}}^T \begin{bmatrix} \boldsymbol{M} & \boldsymbol{0}_{3\times 3} \\ \boldsymbol{0}_{3\times 3} & \boldsymbol{J} \end{bmatrix} \boldsymbol{B_0}\dot{\boldsymbol{\omega}} = \boldsymbol{B}_{\boldsymbol{0}}^T(\boldsymbol{g}_d + \boldsymbol{g}_p) \\ - \boldsymbol{B}_{\boldsymbol{0}}^T \begin{bmatrix} -m\boldsymbol{g}_{gravity} \\ \tilde{\boldsymbol{\omega}}\boldsymbol{J}\boldsymbol{\omega} \end{bmatrix} - \boldsymbol{B}_{\boldsymbol{0}}^T \begin{bmatrix} \boldsymbol{M} & \boldsymbol{0}_{3\times 3} \\ \boldsymbol{0}_{3\times 3} & \boldsymbol{J} \end{bmatrix} \dot{\boldsymbol{B}}_{\boldsymbol{0}}\boldsymbol{\omega} \end{aligned} \tag{16}$$

Given the terrain model $Q(x_C, y_C, z_C)$, we rely on Eq. 16 for simulating the robot dynamics. However, when dealing with unknown terrains, we need to estimate the friction force of the terrain. This friction term will be used in the dynamics modeling in Eq. 6 and as a feed-forward term in our controller (to be discussed in the next section).

Friction Modeling: A friction model, designed for optimal control and real-time dynamic applications, is introduced by Brown and McPhee [17]. In their work, a continuous friction model is defined as a function of relative contact velocity. This model captures the main velocity dependent characteristics of friction: the Stribeck effect and viscous friction. Micro displacement and other additional phenomena of friction such as time dependence of friction are not modeled to avoid the complexity of the model. The magnitude of the friction force (the direction is the opposite of the velocity vector at the contact point), using the model discussed in Brown et al. [17], can be expressed as

$$\begin{aligned} ||\boldsymbol{f}_f|| = f_n\mu_d \tanh(4vv_t^{-1}) + \mu_v v \tanh(4f_n f_{nt}^{-1}) \\ + f_n(\mu_s - \mu_d)\frac{vv_t^{-1}}{(\frac{1}{4}(vv_t^{-1})^2 + .75)^2} \end{aligned} \tag{17}$$

where all the parameters used in the above equation are scalar. The term f_n is the normal force, f_{nt} is the transition force, μ_s, μ_d, and μ_v are the coefficients of static, dynamic, and viscous friction, respectively. The parameter v is the magnitude of the relative velocity at the contact point of the Rollocopter with the ground, v_t is the transition speed coefficient. The three summands in Eq. 17 demonstrate the contributions of dynamic, static, and viscous friction, respectively. This model is continuities and differentiable. Therefore, it is well-suited to optimal control, or multi-body simulations. The reader can refer to work by Brown and McPhee [17] for more details about evaluating the parameters used in Eq. 17.

3. CONTROL STRATEGY

In this section, we discuss a control framework for the Rollocopter. The configuration of the six propellers in the Rollocopter design is capable of providing force and torque in any direction (Figure 1) and allows for separation of position and attitude control in flight mode. Leveraging this separation, we compute the propellers' desired force ($\boldsymbol{f_p}$) to follow a desired position via constructing a feedback linearization based controller [18]. To find the desired propellers' torque ($\boldsymbol{\eta_p}$), we rely on a nonlinear quaternion-based attitude control approach provided in [19]. After finding $\boldsymbol{f_p}$ and $\boldsymbol{\eta_p}$, the angular velocity of each propeller is calculated using Eq. 4. Figure 4 depicts the overall control scheme.

Position Control

To develop the position controller, we first extract the translational equations of motion from Eq. (6)

$$\begin{aligned} \boldsymbol{M}\ddot{\boldsymbol{r}}_P = -m\boldsymbol{g}_{gravity} + \boldsymbol{f}_p + \boldsymbol{f}_d + \delta\boldsymbol{f}_c \\ \boldsymbol{f}_c = \boldsymbol{f}_{cn} + \boldsymbol{f}_f \end{aligned} \tag{18}$$

where δ is zero when the vehicle is flying and is one when the vehicle is on the ground. First, we detail the position control strategy developed for the case in which the robot is rolling.

Rolling Mode: The array of constraint forces $\boldsymbol{f}_c$ in Eq. 18 is comprised of two terms. The array of the normal reaction force of the ground $\boldsymbol{f}_{cn}$ and friction force $\boldsymbol{f}_f$ (which is estimated in Eq. 17). In order to eliminate the effects of the unknown normal reaction force $\boldsymbol{f}_{cn}$, the Eq. 18 is projected onto the space of admissible translational motion using projection matrix $\boldsymbol{B_1} \in R^{3\times 2}$, where matrix $\boldsymbol{B}_{\boldsymbol{1}}^T$ projects any column vector $\in R^3$ onto the tangent plane created by vectors ($\boldsymbol{S_{tan_1}}$ and $\boldsymbol{S_{tan_2}}$ shown in Figure 3). By defining the terrain on which the vehicle rolls on as $z_C = H(x_C, y_C)$, we follow [16] to find the matrix $\boldsymbol{B_1}$ expressed as

$$\boldsymbol{B_1} = \begin{bmatrix} \mathbf{I_2} \\ \nabla z_C \end{bmatrix} \tag{19}$$

By left multiplying the matrix $\boldsymbol{B}_{\boldsymbol{1}}^T$ to Eq. 18 and considering the fact that $\boldsymbol{B}_{\boldsymbol{1}}^T\boldsymbol{f}_{cn} = \boldsymbol{0}$, the modified equation of motion can be expressed as

$$\boldsymbol{B}_{\boldsymbol{1}}^T\boldsymbol{M}\ddot{\boldsymbol{r}}_P = \boldsymbol{B}_{\boldsymbol{1}}^T(-m\boldsymbol{g}_{gravity} + \boldsymbol{f}_p + \boldsymbol{f}_d + \boldsymbol{f}_f) \tag{20}$$

Defining the prescribed position vector as $\boldsymbol{r}_{Pd}(t)$, the tracking error at the position level is expressed as

$$\boldsymbol{e}(t) = \boldsymbol{r}_{Pd}(t) - \boldsymbol{r}_P(t) \tag{21}$$

Following the work in [18], the desired propellers' force generated by the position controller for the rolling mode is

$$\begin{aligned} \boldsymbol{f}_p = &\boldsymbol{M}(\ddot{\boldsymbol{r}}_{Pd}(t) + \boldsymbol{K}_v\dot{\boldsymbol{e}}(t) + \boldsymbol{K}_p\boldsymbol{e}(t) + \boldsymbol{K}_I\int_0^t \boldsymbol{e}(t)) \\ &+ m\boldsymbol{g}_{gravity} - \boldsymbol{f}_f - \boldsymbol{f}_d, \end{aligned} \tag{22}$$

Substituting this total force into Eq. 20, the closed-loop translational dynamic equation of the system can be simplified to

$$\boldsymbol{B}_{\boldsymbol{1}}^T\boldsymbol{M}\left[\ddot{\boldsymbol{e}}(t) + \boldsymbol{K}_v\dot{\boldsymbol{e}}(t) + \boldsymbol{K}_p\boldsymbol{e}(t) + \boldsymbol{K}_I\int_0^t \boldsymbol{e}(t)\right] = \boldsymbol{0} \tag{23}$$

where $\boldsymbol{K}_v$, $\boldsymbol{K}_p$, and $\boldsymbol{K}_I$ are diagonal gain matrices. It can be shown that the system's closed-loop equation (Eq. 23) is asymptotically stable and satisfies the Lyapunov stability conditions as long as the gain matrices are positive definite matrices [18], [20].

Flying Mode: When Rollocopter is flying there is no contact between the shell and the surface. Consequently, the array

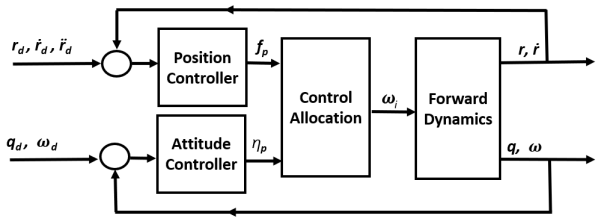

Figure 4: Control scheme used to control the rolling and flying motion of the Rollocopter.

of constraint forces $\boldsymbol{f}_c$ is zero. Therefore, the translational equations of motion provided in Eq. 18 can be expressed as:

$$\boldsymbol{M}\ddot{\boldsymbol{r}} = -m\boldsymbol{g}_{gravity} + \boldsymbol{f}_p + \boldsymbol{f}_d \tag{24}$$

The desired propellers' force $\boldsymbol{f}_p$ generated by the position controller for the flying mode is defined as

$$\boldsymbol{f}_p = \boldsymbol{M}\left[\ddot{\boldsymbol{r}}_d(t) + \boldsymbol{K}_v\dot{\boldsymbol{e}}(t) + \boldsymbol{K}_p\boldsymbol{e}(t) + \boldsymbol{K}_I\int_0^t \boldsymbol{e}(t)\right] + m\boldsymbol{g}_{gravity} - \boldsymbol{f}_d \tag{25}$$

by substituting $\boldsymbol{f}_p$ in Eq. 24, the closed-loop translational dynamics equations for flying can be evaluated as

$$\ddot{\boldsymbol{e}}(t) + \boldsymbol{K}_v\dot{\boldsymbol{e}}(t) + \boldsymbol{K}_p\boldsymbol{e}(t) + \boldsymbol{K}_I\int_0^t \boldsymbol{e}(t) = \boldsymbol{0} \tag{26}$$

This system is asymptotically stable as long as the gain matrices $\boldsymbol{K}_v$, $\boldsymbol{K}_p$, and $\boldsymbol{K}_I$ are positive definite.

Attitude Control

Flying Mode: For attitude control in flying mode, we rely on a quaternion-based approach proposed in [21].

Rolling Mode: The same attitude control approach used for flying can be used in the rolling case. In this case, the torque applied to the system caused by the friction force defined in Eq. 17 can be treated as an external disturbance. After evaluating the required propeller torque $\boldsymbol{\eta}_p$ for attitude control and the required propeller force $\boldsymbol{f}_p$ for position control (Eq. 22 for rolling or Eq. 25 for flying), the angular velocity of each propeller ω_i can be calculated using Eq. 4.

4. Power Consumption Analysis

One of the main advantages of using Rollocopter is its ability to roll/slip on the ground in order to reduce energy consumption. This section provides an analysis of the energy usage of the system in both aerial and terrestrial modes.

Rolling Energetics: To analyze the energetics, without loss of generality, we write the dynamics equation for a general two-dimensional case using Lagrange equations. Then, the required force is calculated for a rolling case, where Rollocopter is rolling with a constant linear velocity of $\boldsymbol{v}_f$ on a flat surface (and along a straight line) with zero slope.

The Lagrange equation is written as

$$\frac{d}{dt}\left(\frac{\partial L}{\partial \dot{\bar{q}}_k}\right) - \left(\frac{\partial L}{\partial \bar{q}_k}\right) = Q_{\bar{q}_k} + \lambda\left(\frac{\partial \phi}{\partial \bar{q}_k}\right) \tag{27}$$

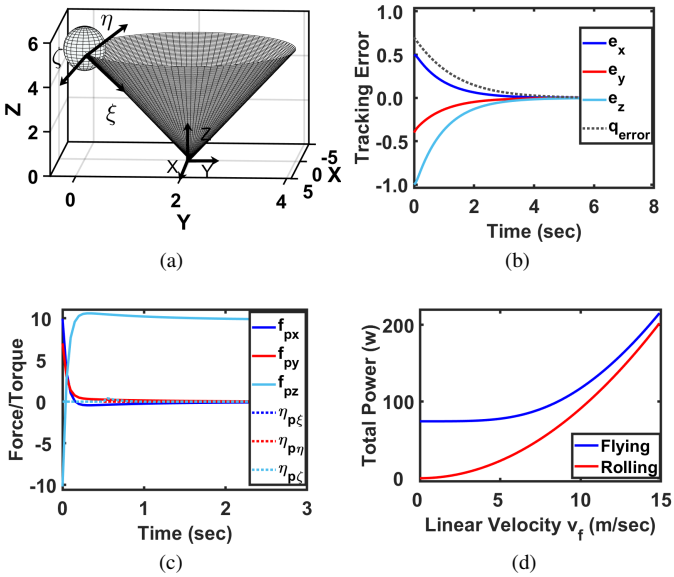

Figure 5: (a) Rollocopter rolling on the top edge of the cone (with the ξ axis pointing at the vertex of the cone), (b) Position and attitude tracking error, (c) Controller input, (d) Required power

Symbol	*Meaning*	*Value*
β_1	Power consumption coeff.	$1.0\ WN^{-2}$
β_2	Power consumption coeff.	$0.1\ WN^{-1}$
R	Rollocopter's radius.	$0.25\ m$
m	Rollocopter's mass.	$1.0\ kg$

Table 1: Relevant model parameters for the Rollocopter, used for the simulation results of the energy-efficiency analysis and the controller validation.

where $\bar{q}_k$ is the generalized coordinate, L is the Lagrangian, ϕ is the rolling constraint, λ is the Lagrange multiplier corresponding to the rolling constraint, and $Q_{\bar{q}_k}$ is the external force $\boldsymbol{f}_P$. Using Eq. 27, the required propeller force to achieve the desired rolling speed, $\boldsymbol{v}_f$, is

$$\boldsymbol{f}_p = -\boldsymbol{f}_d = \frac{1}{2}\bar{\rho}_{den}C_dA_d||\boldsymbol{v}_f||^2\boldsymbol{u}_{\boldsymbol{v}_f} \tag{28}$$

Flying Energetics: When flying along a straight line (zero slope) with a constant linear velocity of $\boldsymbol{v}_f$, the magnitude of the propellers force $\boldsymbol{f}_p$ can be calculated as

$$||\boldsymbol{f}_p|| = \sqrt{(\frac{1}{2}\bar{\rho}_{den}C_dA_d||\boldsymbol{v}_f||^2)^2 + (m||\boldsymbol{g}_{gravity}||)^2} \tag{29}$$

Power consumption: The power consumption of the i-th propeller P_i is modeled similar to [11] as

$$P_i = \beta_1||\boldsymbol{f}_{p_i}||^2 + \beta_2||\boldsymbol{f}_{p_i}|| \tag{30}$$

with propeller-specific constants β_1 and β_2.

5. Simulation Results

In this section, the simulation results for dynamics and control of the vehicle is provided in addition to an energy com-

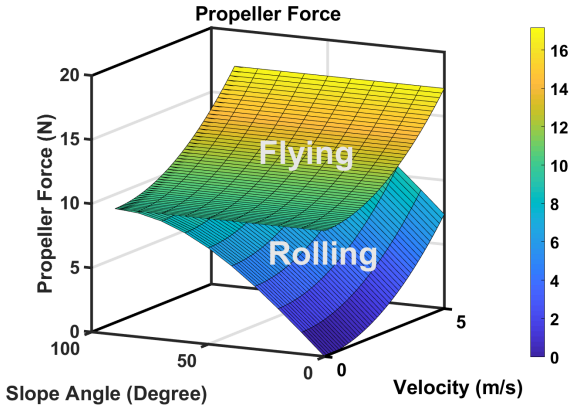

Figure 6: Required rolling force vs. flying force

parison between rolling and flying. The model parameters used for the simulated results are collected in Table 1.

Dynamics and Control: A tracking problem is defined, where the Rollocopter needs to move along a circle in 3D (Figure 5a) with a linear velocity of 1 m/s. While tracking the circle, the axis ξ (of the body frame B_f) needs to point at the vertex of the cone. The control algorithm developed for the flying mode in Section 3 is used and the simulation results are provided. Figure 5b shows the position error and the angle component of the attitude tracking error quaternion q_{error} (in radian). Denoting the desired quaternion as q_d and the vehicle quaternion with q_v, the attitude tracking error is defined as $q_{error} = q_v^{-1}.q_d$. It can be observed that after approximately four seconds the position and attitude error converges to zero. Figure 5c shows the exerted propeller force $\boldsymbol{f}_p$ (in Newton) and torque $\boldsymbol{\eta}_p$ (in Newton Meter) over time (the values of $\boldsymbol{\eta}_{p_\xi}$ and $\boldsymbol{\eta}_{p_\eta}$ are negligible).

Energy Analysis: Equations 28 and 29 are used to evaluate the required force for flying and rolling on a straight line with zero slope. The required power at different speeds is evaluated using Eq. 30 and shown in Figure 5d. As observed in the figure, flying consumes a significantly higher power, specifically at low speeds, compared to rolling. Figure 6 demonstrates the required propeller force at different speeds and slope angles. Where the slope angle is measured from the horizon. It can be observed that the required force for rolling is smaller than the flying forces. The advantage of rolling over flying decreases as the translational velocity or slope increases and the forces become equal when the slope is 90^0. It needs to be mentioned that rolling will become more challenging as the terrain transfers from a smooth plane into a rough or uneven one. More detail on the energy analysis and path planning for uneven surfaces will be provided in forthcoming research.

6. Conclusion and Future Work

In this work, the design and modeling of a new hybrid aerial-ground mobility system for extreme terrains referred to as Rollocopter was provided. The main features of the proposed mobility system are its energy-efficiency, collision resiliency, and precise controllability. A dynamics model that considers the terramechanics of the vehicle is introduced as well as a hybrid control algorithm for rolling and flying mode. It was shown that the Rolling mode could significantly improve the efficiency of the vehicle specifically on low speeds.

Future Work

Terramechanics: During the terrestrial experiments of Rollocopter in different mediums, friction forces had a great impact on the system dynamics. Therefore, an accurate terramechanics model is important for precise modeling. Authors are currently working on online adaptation to terrain parameters.

Energy Saving With Locking Control: The discussed variant of the Rollocopter system encloses a hexacopter which is fixed to the outer shell. In an enhanced variant of Rollocopter, we connect the hexacopter to the outer shell via bearing (see Figure 1) that can be locked and unlocked. This will change the dynamics of the system and essentially affect the required force/power to roll on the ground.

Acknowledgments

This research was partially carried out at the University of Arizona and Jet Propulsion Laboratory under a contract with the National Aeronautics and Space Administration. U.S. Government sponsorship acknowledged.

References

[1] R. Bähnemann, D. Schindler, M. Kamel, R. Siegwart, and J. Nieto, "A decentralized multi-agent unmanned aerial system to search, pick up, and relocate objects," in *Proceedings of 2017 IEEE International Symposium on Safety, Security and Rescue Robotics (SSRR)*. IEEE, 2017, p. 8088150.

[2] M. Nieuwenhuisen, M. Beul, R. A. Rosu, J. Quenzel, D. Pavlichenko, S. Houben, and S. Behnke, "Collaborative object picking and delivery with a team of micro aerial vehicles at mbzirc," in *Mobile Robots (ECMR), 2017 European Conference on*. IEEE, 2017, pp. 1–6.

[3] S. Herwitz, L. Johnson, S. Dunagan, R. Higgins, D. Sullivan, J. Zheng, B. Lobitz, J. Leung, B. Gallmeyer, M. Aoyagi *et al.*, "Imaging from an unmanned aerial vehicle: agricultural surveillance and decision support," *Computers and electronics in agriculture*, vol. 44, no. 1, pp. 49–61, 2004.

[4] A. Agha-mohammadi, N. K. Ure, J. P. How, and J. Vian, "Health aware stochastic planning for persistent package delivery missions using quadrotors," in *International Conference on Intelligent Robots and Systems (IROS)*, Chicago, IL, September 2014, pp. 3389–3396.

[5] A. Tagliabue, M. Kamel, S. Verling, R. Siegwart, and J. Nieto, "Collaborative transportation using mavs via passive force control," in *Robotics and Automation (ICRA), 2017 IEEE International Conference on*. IEEE, 2017, pp. 5766–5773.

[6] B. Balaram, T. Canham, C. Duncan, H. F. Grip, W. Johnson, J. Maki, A. Quon, R. Stern, and D. Zhu, "Mars helicopter technology demonstrator," in *2018 AIAA Atmospheric Flight Mechanics Conference*, 2018, p. 0023.

[7] P. Turtle, J. Barnes, M. Trainer, R. Lorenz, S. MacKenzie, K. Hibbard, D. Adams, and P. Bedini, "Dragonfly: Exploring titan's prebiotic organic chemistry and habitability. e." *Icarus*, vol. 243, pp. 191–207, 2007.

[8] "Shapeshifters from science fiction to science fact: Globetrotting from titan's rugged cliffs to its deep seafloors," https://www.nasa.gov/directorates/spacetech/niac, March 2018.

[9] K. Karydis and V. Kumar, "Energetics in robotic flight at small scales," *Interface focus*, vol. 7, no. 1, p. 20160088, 2017.

[10] S. Verling, B. Weibel, M. Boosfeld, K. Alexis, M. Burri, and R. Siegwart, "Full attitude control of a vtol tailsitter uav," in *Robotics and Automation (ICRA), 2016 IEEE International Conference on*. IEEE, 2016, pp. 3006–3012.

[11] A. Kalantari and M. Spenko, "Modeling and performance assessment of the hytaq, a hybrid terrestrial/aerial quadrotor," *IEEE Transactions on Robotics*, vol. 30, no. 5, pp. 1278–1285, 2014.

[12] A. Briod, P. Kornatowski, J.-C. Zufferey, and D. Floreano, "A collision-resilient flying robot," *Journal of Field Robotics*, vol. 31, no. 4, pp. 496–509, 2014.

[13] V. Lippiello and F. Ruggiero, "Cartesian impedance control of a uav with a robotic arm." 2012.

[14] D. Brescianini and R. D'Andrea, "Design, modeling and control of an omni-directional aerial vehicle," in *Robotics and Automation (ICRA), 2016 IEEE International Conference on*. IEEE, 2016, pp. 3261–3266.

[15] M. Kamel, S. Verling, O. Elkhatib, C. Sprecher, P. Wulkop, Z. J. Taylor, R. Siegwart, and I. Gilitschenski, "The voliro omnidirectional hexacopter: An agile and maneuverable tiltable-rotor aerial vehicle," *IEEE Robotics & Automation Magazine*, 2018.

[16] P. E. Nikravesh, "Systematic reduction of multibody equations of motion to a minimal set," *International Journal of Non-Linear Mechanics*, vol. 25, no. 2-3, pp. 143–151, 1990.

[17] P. Brown and J. McPhee, "A continuous velocity-based friction model for dynamics and control with physically meaningful parameters," *Journal of Computational and Nonlinear Dynamics*, vol. 11, no. 5, p. 054502, 2016.

[18] F. L. Lewis, D. M. Dawson, and C. T. Abdallah, *Robot Manipulator Control: Theory and Practice*. Marcel Dekker, Inc, 2003.

[19] R. A. Paielli and R. E. Bach, "Attitude control with realization of linear error dynamics," *Journal of Guidance, Control, and Dynamics*, vol. 16, no. 1, pp. 182–189, 1993.

[20] S. Sabet and M. Poursina, "Computed torque control of fully-actuated nondeterministic multibody systems," *Multibody System Dynamics*, vol. 41, no. 4, pp. 347–365, Dec 2017. [Online]. Available: https://doi.org/10.1007/s11044-017-9577-4

[21] H. Schaub, M. R. Akella, and J. L. Junkins, "Adaptive control of nonlinear attitude motions realizing linear closed loop dynamics," *Journal of Guidance, Control, and Dynamics*, vol. 24, no. 1, pp. 95–100, 2001.

BIOGRAPHY

Sahand Sabet *received his B.S. in mechanical engineering from Shiraz University, Fars province, Iran, and a M.S. in mechanical engineering (dynamics and control) from University of Arizona, in 2013 and a 2016, respectively. Currently, he is a Ph.D. candidate at University of Arizona under professor Parviz E. Nikravesh, with a focus multibody dynamics. His research explores dynamics modeling of multibody systems as well as control and modeling of vehicles with nonholonomic constraints.*

Dr. Ali-Akbar Agha-Mohammadi *is a Robotics Research Technologist with NASA's Jet Propulsion Laboratory (JPL), Caltech. Previously, he held a position of a Autonomy Research Engineer with Qualcomm Research and a Postdoctoral Researcher with the Laboratory for Information and Decision Systems at Massachusetts Institute of Technology. He received his Ph.D. from Texas A&M University, College Station, TX. His research interests include robotic autonomy, mobility and perception, stochastic control systems, and filtering theory. Dr. Agha named as a NASA NIAC Fellow in 2018.*

Andrea Tagliabue *is a Robotics Engineer at California Institute of Technology/NASA's Jet Propulsion Laboratory. He received a B.S. with honours in Automation Engineering from Politecnico di Milano, and a M.S. in Robotics, Systems and Control from ETH Zurich. During his master, he was visiting researcher at U.C. Berkeley and research assistant at the ETH's Autonomous Systems Lab. Prior to that, he worked at ABB under the "dream-internship" talent program. His research interests include motion planning, control, and localization for Micro Aerial Vehicles.*

D. Sawyer Elliott *graduated from Rochester Institute of Technology with a Bachelor of Science in Mechanical Engineering in 2015. During his undergraduate career he worked at M.I.T. Lincoln Laboratory, where he worked on small spacecraft for weather sensing. Currently, he is a Ph.D. candidate at Cornell University under Professor Mason Peck, with a focus on dynamics and controls. While at Cornell University he worked on a small spacecraft project with the goal of autonomously docking two CubeSats. His current research explores control methods for momentum control systems, as well as the control of gyroscopically actuated robotic systems and their applications for exploration of extreme terrain.*

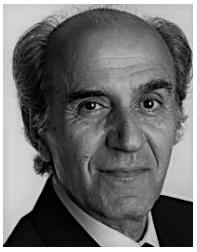

Parviz E. Nikravesh *is a Professor of Aerospace and Mechanical Engineering at The University of Arizona. He earned his Doctorate degree from Tulane University in 1976. He received an Honorary Doctorate from the Technical University of Lisbon in 2001. He has published more than one hundred papers and several textbooks. His main research interest is in computational methods in multibody dynamics and its applications.*